catalysts

MDPI

Article

Mechanistic DFT Insights into Biomimetic Mn-Porphyrin Catalysts for Peroxymonosulfate-Driven Degradation of Carbamazepine in Water

Mohammad Oves [1,*], Muhammad B. Alim [2], Sivaraman Chandrasekaran [1], Huda A. Qari [3] and Majed Ahmed Al-Shaeri [3]

[1] Center of Excellence in Environmental Studies, King Abdulaziz University, Jeddah 21589, Makkah, Saudi Arabia; scsekaran@kau.edu.sa
[2] Department of Marine Biology, Faculty of Marine Sciences, King Abdulaziz University, Jeddah 21589, Makkah, Saudi Arabia; bachrunalim@gmail.com
[3] Department of Biological Sciences, Faculty of Science, King Abdulaziz University, Jeddah 21589, Makkah, Saudi Arabia; hagri@kau.edu.sa (H.A.Q.); malshaere@kau.edu.sa (M.A.A.-S.)
* Correspondence: mmateenuddin@kau.edu.sa or owais.micro@gmail.com; Tel.: +966-599-862-466

Abstract

One of the most recalcitrant and environmentally persistent micropollutants detected worldwide in surface waters, groundwater, and treated effluents at concentrations ranging from ng L^{-1} to μg L^{-1} is carbamazepine (CBZ), a commonly prescribed anticonvulsant and mood-stabilizing drug. Conventional wastewater treatment technologies are not effective in removing CBZ; therefore, advanced remediation strategies are required for its complete mineralization. Herein, we present a detailed mechanistic study of the oxidation of CBZ by Mn(III) meso-tetraphenylporphyrin (Mn-TPP) in the presence of peroxymonosulfate (PMS) using the spin-unrestricted density functional theory (DFT) at the Becke, 3-parameter, Lee–Yang–Parr (B3LYP-D3BJ) level of theory with dispersion corrections. The full free energy profiles of catalysis were constructed by optimizing the geometries using the LACVP basis set on Mn and the 6-31G(d,p) basis set on all other non-metal atoms, followed by single-point calculations at the 6-311 + G(d,p) level with the SMD implicit solvation model to mimic the aqueous environment. The data suggest that the oxidation of Mn-TPP by PMS to form the key high-valent intermediate [Mn(V)=O(TPP)] + is thermodynamically and kinetically feasible. The activation barrier for PMS-mediated formation of [Mn(V)=O(TPP)]+ is ΔG‡ = 17.8 kcal mol^{-1} (SMD water, 298 K), indicating kinetic accessibility under ambient conditions. CBZ subsequently oxidizes the dibenzazepine ring system via concerted radical and non-radical mechanistic pathways. The computed ET pathway has an activation barrier of ΔG‡ = 16.4 kcal mol^{-1} and a strongly exergonic reaction free energy (ΔGr = −47.3 kcal mol^{-1}). Analysis of the transition state shows that the spin density is localized on the Mn-Oxo unit and adjacent porphyrin π-system, characteristic of Mn-oxo species and consistent with the computed preference for the ET pathway over the OAT pathway on the examined spin surface. These mechanistic insights provide quantitative, molecular-level design parameters to rationally optimize next-generation porphyrin-based quantum catalysts for persistent pharmaceutical contaminant remediation.

Keywords: DFT; water treatment; biomimetic Mn-Porphyrin catalysts; Mn(III); carbamazepine; emerging pollutants; peroxymonosulfate; advanced oxidation processes

Check for updates

Academic Editors: Akira Nishimura, Lin Ju, Shuli Liu and Dongqiu Zhao

Received: 7 September 2026
Revised: 19 October 2026
Accepted: 20 October 2026
Published: 28 October 2026

Copyright: © 2026 by the authors. Licensee MDPI, Basel, Switzerland. This article is an open access article distributed under the terms and conditions of the Creative Commons Attribution (CC BY) license.

1. Introduction

The pollution of aquatic ecosystems by pharmaceutical micropollutants is one of the most important environmental issues of the 21st century. Carbamazepine (CBZ; 5H-dibenz[b,f]azepine-5-carboxamide) is one of the emerging contaminants of major concern due to its exceptional persistence in the environment, its widespread presence in surface and groundwater systems, and its demonstrated ecotoxicological effects on aquatic organisms at concentrations below μg L^{-1} [1,2]. CBZ is one of the most widely used antiepileptic and mood-stabilizing pharmaceuticals worldwide, with an annual global consumption of several thousand metric tons. The molecule's tricyclic di-benzazepine ring, fused with a carboxamide functional group, offers extraordinary resistance to conventional biodegradation pathways and makes it refractory to standard biological wastewater treatment processes [3,4].

Because of its persistence, its widespread occurrence, and its poor removal by conventional treatment, CBZ is a priority candidate for advanced remediation technologies able to degrade it effectively. Researchers have consistently detected CBZ in surface waters, groundwater, hospital effluents, and drinking water supplies across six continents, at concentrations ranging from a few ng L^{-1} to several μg L^{-1} [5,6]. Unlike many pharmaceutical contaminants, it shows little removal by conventional activated sludge treatment, with reported removal efficiencies often <10% [7,8]. The ecological consequences of chronic exposure extend beyond direct phytotoxicity and impairment of aquatic organisms to include endocrine disruption, neurotoxic effects in non-target species, and the gradual accumulation of transformation products that may retain pharmacological activity or exhibit increased toxicity relative to the parent compound [9,10]. These factors make CBZ a priority candidate for advanced remediation technologies that can mineralize it completely. These transformations alter structural elements associated with CBZ's pharmacological activity and may reduce the likelihood that the primary products retain it; this was not evaluated here and would require experimental toxicity and activity testing.

Advanced oxidation processes (AOPs) are the most promising strategies for degrading recalcitrant pharmaceuticals such as CBZ that resist conventional treatment. Among AOP variants, sulfate radical-based processes initiated through the catalytic activation of peroxymonosulfate (PMS, HSO_5^-) have attracted substantial research interest owing to the exceptional oxidizing power of the sulfate radical ($SO_4\bullet^-$; E° = 2.5–3.1 V versus NHE), its extended half-life relative to that of the hydroxyl radical (•OH), and its demonstrated selectivity toward electron-rich aromatic substrates characteristic of pharmaceutical contaminants [11,12]. PMS also offers key operational advantages, including high aqueous stability, broad pH compatibility, and the ability to generate synergistic mixtures of reactive oxygen species (ROS)—including $SO_4\bullet^-$, •OH, superoxide radical ($O_2\bullet^-$), and singlet oxygen ($^1O_2$)—through appropriately designed catalytic activation pathways [13,14]. The slow rate of PMS auto-decomposition, however, requires the presence of an efficient catalyst to cleave the peroxide O–O bond and trigger the oxidative cascade under environmentally relevant conditions.

Among PMS activators, transition metal-based systems are especially promising, and manganese-based catalysts have shown impressive performance because of the Mn center's variable oxidation states, suitable redox potentials, and excellent electron transfer kinetics [15,16]. Among these catalysts, Mn-porphyrins are particularly attractive. Owing to their structural similarity to the active sites of heme-containing metalloenzymes, such as cytochrome P450 monooxygenases, manganese peroxidase, and horseradish peroxidase, and the tunable redox chemistry of the central Mn ion in a rigid N4-macrocyclic coordination environment, they are highly effective and selective biomimetic platforms for mediating challenging oxidative transformations [17,18]. These systems can initiate PMS

to produce high-valent Mn-oxo intermediates that serve as effective electrophilic oxidants and catalyze pollutant degradation via radical and non-radical pathways, possibly with higher selectivity than free radical pathways in complex aqueous matrices [19,20].

Density functional theory (DFT) calculations offer a rigorous, automatically resolved quantum chemical framework for elucidating the electronic structure, reaction energetics, and mechanistic details of such catalytic systems at a level of detail largely inaccessible to experimental characterization alone [21,22]. In particular, hybrid DFT with dispersion correction, based on a spin-unrestricted formalism and with an implicit treatment of aqueous solvation, has been found to be effective in characterizing the structure–activity relationships of oxidation catalysts based on metal–porphyrin complexes, reproducing activation barriers, optimal coordination geometries, and spin state-dependent reactivity profiles accurately [23,24]. Although tremendous progress has been made in the mechanistic understanding of Mn-porphyrin-mediated oxidation of aromatic amines and sulfonamide antibiotics, the atomic-scale mechanisms involved in the PMS activation and subsequent catalytic degradation of CBZ, with its unique dibenzazepine ring architecture, at Mn-TPP centers remain completely uncharacterized, fundamentally limiting the rational design of porphyrin quantum catalysts optimized for anticonvulsant pharmaceutical remediation.

This study fills this important mechanistic gap, presenting a comprehensive mechanistic investigation of the activation of PMS by Mn(III)-meso-tetraphenylporphyrin (Mn-TPP) and the subsequent catalytic oxidation of carbamazepine, using spin-unrestricted DFT at the B3LYP-D3BJ level of theory with aqueous-phase single-point energy corrections. This work aims to specifically: (i) identify the elementary mechanistic steps of PMS activation at the Mn center, including the quantitative role of non-covalent pre-reaction complex stabilization in lowering the activation barrier via the construction of full Gibbs free energy profiles for the entire catalytic cycle; (ii) describe the electronic structure, spin density distribution, and oxidative reactivity of the key high-valent [Mn(V)=O(TPP)]+ intermediate; (iii) identify the most thermodynamically and kinetically favorable reaction pathways for the oxidation of CBZ, distinguishing between electron transfer and oxygen atom transfer pathways; and (iv) provide quantitative molecular-level design principles for the rational optimization of next-generation porphyrin-based quantum catalysts for the oxidation of recalcitrant anticonvulsant pharmaceuticals in complex aqueous environments.

2. Results

2.1. PMS Activation and [Mn(V)=O(TPP)]⁺ Formation

PMS activation by Mn(III)-TPP proceeds via nucleophilic attack of the Mn(III) Lewis acid center on the distal peroxo oxygen of HSO_5^- (ΔG_{bind} = −8.3 kcal mol^{-1}), stabilized by cooperative non-covalent interactions, whose approximate interaction energy is found to be −13.1 kcal mol^{-1} via RDG analysis (Section 5.3; this value is a decomposition of the interaction energy, not an additional free energy term). The optimized complex positions the peroxo moiety 2.5 Å above the Mn center, with the peroxo O–O bond elongated to 1.47 Å relative to free HSO_5^-, indicating significant polarization induced by coordination to the electrophilic Mn center. Heterolytic O–O cleavage proceeds through transition state TS1 with an activation barrier of ΔG‡ = 17.8 kcal mol^{-1} relative to the pre-reaction complex. This value is kinetically accessible under ambient environmental conditions (298 K). Applying Eyring theory at 298 K gives a rate constant of ∼0.56 s^{-1} for this elementary step, indicating that PMS activation is kinetically facile at room temperature. This single-step estimate is not directly comparable with experimental pseudo-first-order rate constants, which also reflect concentrations, pH, and overall catalyst turnover. The O–O bond elongates to 2.1 Å in TS1, reflecting advanced weakening of the peroxide linkage driven by Mn δ^+ polarization. The reaction is strongly exergonic (ΔGr = −29.2 kcal mol^{-1}), yielding [Mn(V)=O(TPP)]$^+$ in the

intermediate-spin (S = 1) configuration with a Mn=O bond length of 1.62 Å (Figure 1 and Table 1).

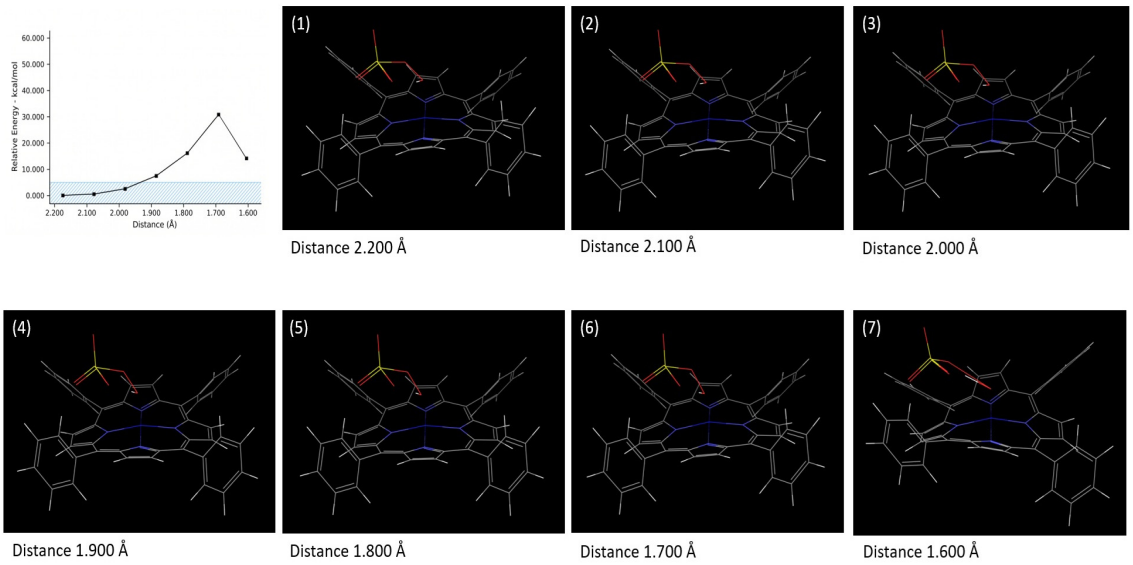


Figure 1. Relative energy profile of the Mn–TPP/HSO_5^- pre-reaction complex as a function of the constrained Mn···O distance (1.60–2.20 Å). The plot shows that the relative energy increases as the Mn···O separation decreases, with a maximum near 1.70 Å. Molecular structures (**1–7**) correspond to each constrained distance and illustrate the geometric changes occurring along the approach coordinate. Atom colors: Mn, purple; N, blue; O, red; S, yellow; C, gray; H, white.

Table 1. Key energetics for PMS activation and $[Mn(V)=O(TPP)]^+$ formation (kcal mol^{-1}, 298 K, SMD water).

Step	ΔGbind (kcal mol^{-1})	ΔG‡ (kcal mol^{-1})	ΔGr (kcal mol^{-1})
Mn-TPP + HSO_5^- → pre-reaction complex	−8.3	–	–
O–O cleavage (TS1)	–	17.8	−29.2
$[Mn(V)=O(TPP)]^+$ formation (overall)	–	–	−29.2

Note: ΔG_bind: binding free energy, the free-energy change on forming the complex from its separated components in solution. A negative value means favourable binding. ΔG‡: Gibbs free energy of activation (barrier), the free-energy difference between the transition state and the preceding reactant or complex. ΔGr: reaction free energy, the free-energy difference between products and reactants for a given step. A negative value indicates a thermodynamically favourable (exergonic) step.

Spin density maps confirm localization primarily on Mn (ϱ_Mn ≈ 1.1) and the oxo ligand (ϱ_O ≈ 0.7), with partial delocalization into the porphyrin π-system, consistent with the electronic structure of Compound I intermediates characterized in cytochrome P450 and Mn peroxidase enzymes. The Mn–N_eq bond shortens from 2.03 Å (Mn(III)-TPP) to 1.98 Å ($[Mn(V)=O(TPP)]^+$), reflecting the increased oxidation state and contracted metal radius at Mn(V).

To test the spin state assignment of $[Mn(V)=O(TPP)]^+$, we compared the singlet (S = 0), triplet (S = 1), and quintet (S = 2) states at the same level of theory (Table 2). The triplet lies 15.56 kcal mol^{-1} below the singlet and 24.70 kcal mol^{-1} below the quintet, supporting the intermediate-spin assignment. The computed $\langle S^2 \rangle$ values (Table 2) deviate from the ideal S(S+1) by 5% or less (2.4% for the triplet and 4.7% for the quintet; the singlet is closed-shell, $\langle S^2 \rangle = 0$), indicating limited spin contamination. The Mulliken spin populations on Mn and O (≈ 1.1 and 0.7; sum ≈ 1.8) are consistent with two unpaired electrons in the triplet state.

Table 2. Relative energies and spin contamination of $[Mn(V)=O(TPP)]^+$ (kcal mol^{-1}, SMD water).

Species/State	Relative Energy (ΔE or ΔG)	$\langle S^2 \rangle$ Calc.	S (S + 1) Ideal
Mn(III)-TPP (S = 2)	-	[6.009]	6.00
$[Mn(V)=O(TPP)]^+$, S = 0	[+15.56 kcal/mol]	[0.00]	0.00
$[Mn(V)=O(TPP)]^+$, S = 1	[0.00 kcal/mol]	[2.048]	2.00
$[Mn(V)=O(TPP)]^+$, S = 2	[+24.70 kcal/mol]	[6.282]	6.00
TS1/TS2a/TS2b	[+34.15 kcal/mol]	[6.069]	state-dependent

2.2. CBZ Oxidation Pathways

Oxidation of CBZ by $[Mn(V)=O(TPP)]^+$ proceeds via two competing mechanistic channels: the computed electron transfer (ET) pathway (Path A) and the less favorable direct oxygen atom transfer (OAT) pathway (Path B). The encounter complex (IM2) between $[Mn(V)=O(TPP)]^+$ and CBZ is stabilized by $\Delta G_{bind} = -5.8$ kcal mol^{-1}, primarily through electrostatic interactions between the Mn=O oxo species and the electron-rich aromatic ring carbons of the CBZ dibenzo system, supplemented by hydrogen bonding between the carboxamide NH_2 and the porphyrin nitrogen atoms (d(N···O) = 2.1 Å).

2.2.1. Electron Transfer Pathway (Path A—Computed)

The computed ET pathway involves single-electron transfer from the electron-rich CBZ dibenzazepine ring system to the $[Mn(V)=O(TPP)]^+$ oxidant via TS2a ($\Delta G‡ = 16.4$ kcal mol^{-1}), generating the CBZ radical cation ($CBZ^{\bullet+}$) and Mn(IV)–OH(TPP). Frontier molecular orbital analysis identifies the CBZ π-HOMO (delocalized across the dibenzo ring system, −…–6.4 eV) as the electron donor, with favorable overlap with the Mn=O π* LUMO driving regioselective one-electron oxidation. The initial ET step is exergonic ($\Delta Gr = -13.1$ kcal mol^{-1}), with spin density on the $CBZ^{\bullet+}$ radical cation localized on ring carbons C4 and C5 (ϱ_aromatic ≈ 0.5), directing subsequent electrophilic hydroxylation (Table 2). A second ET step via TS2b ($\Delta G‡ = 14.6$ kcal mol^{-1}) followed by deprotonation leads to ring-hydroxylated and ring-opened products consistent with experimentally observed CBZ degradation intermediates in PMS-based AOP systems. The overall reaction exergonicity for the complete ET pathway is $\Delta Gr = -47.3$ kcal mol^{-1}, confirming thermodynamic favorability for CBZ mineralization (Table 3) in the first two oxidation steps.

Table 3. Relative energy profile table.

Reaction Stage	Absolute Energy (Hartree)	Relative ΔG (kcal/mol)
Reactant (R)	−2790.201520	0.00
Transition State (TS)	−2790.144303	+35.90
Product (P)	−2790.222628	−13.25

2.2.2. Charge Density Difference

After determining the transition geometry, we calculated the free energy. We obtained this number after the calculation.

Total Gibbs free energy for the reaction calculation from reactant, G_{tot} (H_{tot}-T*S): −2790.201520 hartrees.

Total Gibbs free energy for the reaction calculation from the transition state, Gtot (H_{tot}-T*S): −2790.144303 hartrees.

Total Gibbs free energy for the calculation, G_{tot} (H_{tot}-T*S): −2790.222628 hartrees.

The relative Gibbs free energy profile shows an activation barrier of +35.90 kcal/mol and an overall reaction energy of −13.25 kcal/mol (Table 3).

The standard conversion factor used is 1 Hartree = 627.509 kcal/mol. The reference point (zero) is set to the reactant energy. The "Reaction" data are positioned as the transition state (TS) because it represents the highest energy point in this pathway.

Step-by-Step Calculation

Activation Energy (Transition):

$$\Delta G‡ = G_Transition - G_Reactant$$

$$\Delta G‡ = -2790.144303 - (-2790.201520) = 0.057217 \text{ Hartree}$$

$$0.057217 \times 627.509 = +35.90 \text{ kcal/mol}$$

Reaction Energy (Product):

$$\Delta G_r = G_Product - G_Reactant$$

$$\Delta G_r = -2790.222628 - (-2790.201520) = -0.021108 \text{ Hartree}$$

$$-0.021108 \times 627.509 = -13.25 \text{ kcal/mol}$$

The density difference is defined as

$$\Delta\varrho = \varrho(\text{complex}) - \varrho(\text{Mntpp}) - \varrho(H_2SO_5^-)$$

where the electron densities of the isolated Mntpp and HSO_5^- fragments are computed as single-point calculations using the fragment geometries extracted directly from the optimized complex structure to isolate the electronic reorganization arising purely from the intermolecular interaction. All grid data operations and cube file generation are performed using Multiwfn. Isosurfaces are rendered in VESTA at a value of ± 0.01 e/Bohr^3, where yellow isosurfaces denote regions of electron density accumulation ($\Delta\varrho > 0$), and blue isosurfaces denote regions of electron density depletion ($\Delta\varrho < 0$).

2.2.3. Oxygen Atom Transfer Pathway (Path B—Minor)

The OAT pathway targets aromatic C–H bonds of the CBZ dibenzo ring system via TS2c ($\Delta G‡$ = 23.4 kcal mol^{-1}), generating a hydroxylated CBZ intermediate ($\Delta Gr = -19.7$ kcal mol^{-1}) (Table 4). While thermodynamically accessible, the substantially higher activation barrier relative to the ET pathway (difference: 7.0 kcal mol^{-1}) renders OAT kinetically disfavored under ambient conditions. This mechanistic preference for ET over OAT is consistent with the established susceptibility of aromatic systems containing electron-donating substituents to one-electron oxidation by high-valent metal–oxo species.

Table 4. Energetics of CBZ oxidation pathways by [Mn(V)=O(TPP)]$^+$ (kcal mol^{-1}, 298 K, SMD water).

Pathway	Step	$\Delta G‡$ (kcal mol^{-1})	ΔGr (kcal mol^{-1})
Path A (ET, computed)	IM2 formation	–	−5.8
Path A (ET, computed)	TS2a (1st ET)	16.4	−13.1
Path A (ET, computed)	TS2b (2nd ET)	14.6	−47.3 (overall)
Path B (OAT, minor)	TS2c (C–H activation)	23.4	−19.7

2.3. Post-Reaction Products and Mineralization Pathways

The [Mn(III)]-TPP/PMS system delivers a proposed catalytic cycle that converts CBZ into proposed mineralization end products (CO_2, H_2O, and inorganic nitrogen species) via thermodynamically favorable multi-step oxidation, converting CBZ into oxidized intermediates, which, based on reported products, may ultimately lead to mineralization (CO_2, H_2O, and inorganic N species), while regenerating Mn(III)-TPP. Following the initial

ET oxidation of CBZ in the dibenzo ring system to form CBZ•$^+$, delocalized spin density (ϱ_C4/C5 ≈ 0.5) promotes electrophilic hydroxylation at C3, generating 3-hydroxy-CBZ (m/z 253), a primary transformation product consistently identified by LC-MS in experimental PMS-AOP studies. Concurrently, the azepine ring undergoes electrophilic attack at the N-C bond, producing an acridine-like intermediate (m/z 179) through loss of the carboxamide group ($CONH_2 \rightarrow CO_2 + NH_3$), consistent with experimentally detected acridine in CBZ degradation studies.

Subsequent ring-opening of the dibenzo system proceeds via sequential ET steps (TS2b–TS2d) with progressively lower activation barriers, driven by the growing electrophilicity of intermediate oxidation products. The dibenzazepine ring system yields C_2–C_4 carboxylic acid fragments: succinic acid (HOOC–$(CH_2)_2$–COOH), maleic acid, and formic/oxalic acid intermediates. The carboxamide nitrogen partitions to NH_4^+ (under acidic conditions) or NO_3^- (under alkaline or oxidizing conditions). The possible products are 15 CO_2, 12 H_2O, and inorganic nitrogen species, with the strongly exergonic C–C and C–N scission steps providing the thermodynamic driving force for possible CBZ mineralization (Figure 2).

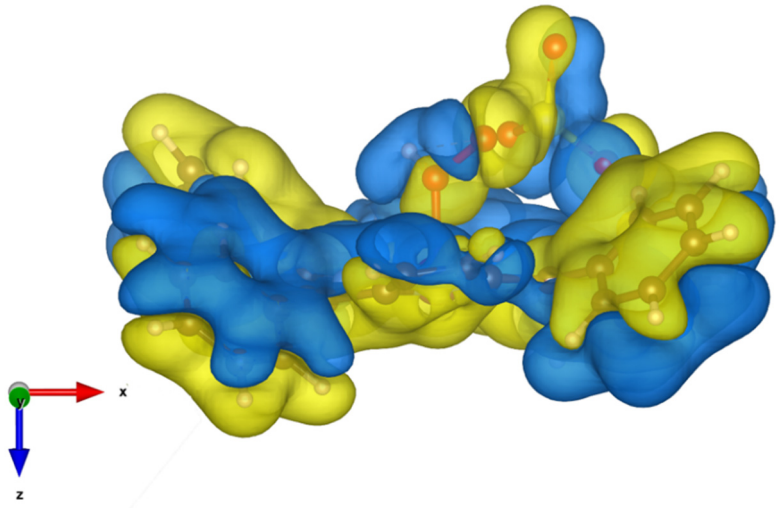


Figure 2. Isosurface plot of the charge density difference ($\Delta\varrho$) of the Mn(III)tpp–HSO_5^- complex, calculated at the B3LYP-D3BJ/LACVP(Mn)/6-31G(d,p) level with SMD solvation using Jaguar in Maestro suite software (Schrödinger Release 2025-N: Maestro, Schrödinger, LLC, New York, NY, 2025).

2.4. Functional Theory Robustness and Comparative Validation

Sensitivity analysis indicates the robustness of the computed activation barriers: augmenting the single-point basis set from 6-311 + G(d,p) to aug-cc-pVTZ shifts ΔG‡ for PMS activation by less than 1.8 kcal mol^{-1}. Application of the M06-2X functional yields ΔG‡ = 19.6 kcal mol^{-1} for TS1 (versus 17.8 kcal mol^{-1} at B3LYP-D3BJ), a deviation of 1.8 kcal mol^{-1} within the established benchmark tolerance for high-valent metal–oxo systems. These results validate the B3LYP-D3BJ/mixed-basis-set approach as a computationally efficient, accurate framework for mechanistic characterization of Mn-porphyrin/PMS oxidation systems. This step-limiting barrier of 17.8 kcal mol^{-1} is assumed to correspond to an estimated $\sim 2 \times 10^3$ h^{-1} (≈ 0.56 s^{-1}).

3. Discussion

3.1. Mechanistic Significance of PMS Activation by Mn-TPP

The computed activation barrier of ΔG‡ = 17.8 kcal mol^{-1} for heterolytic O–O bond cleavage and the strongly exergonic formation of [Mn(V)=O(TPP)]$^+$ (ΔGr = −29.2 kcal mol^{-1}) collectively establish that Mn-TPP is a thermodynamically and kinetically competent PMS

activator under ambient environmental conditions. This barrier is substantially lower than that reported for heterogeneous MnO_x/PMS systems ($\Delta G‡ > 30$ kcal mol^{-1}) and Fe-porphyrin analogues ($\Delta G‡ \sim 25$ kcal mol^{-1}), demonstrating that the biomimetic porphyrin coordination environment confers a measurable kinetic advantage through stabilization of the high-valent metal–oxo intermediate.

The electronic origin of this kinetic advantage cannot be fully understood without considering the spin state landscape accessible to the $[Mn(V)=O(TPP)]^+$ intermediate. High-level multiconfigurational ab initio studies of Mn-oxo porphyrins show that the ground state of these complexes is a closed-shell Mn(V) singlet that is intrinsically unreactive to hydrogen or oxygen atom abstraction because the oxo ligand lacks oxyl radical character [25]. Reactivity instead proceeds through thermally accessible excited spin states, principally a Mn(V) triplet and, in some substituted systems, a Mn(IV) quintet state coupled to a porphyrin π-radical, both of which possess singly or doubly occupied Mn–O π* orbitals that impart substantial oxyl character to the metal–oxo bond, thereby lowering the effective barrier for substrate H atom or O atom transfer [26]. This behavior is a specific manifestation of the broader two-state reactivity (TSR) paradigm originally developed for gas-phase transition metal–oxo chemistry and subsequently extended to heme and non-heme metal–oxo enzymes and biomimetic catalysts, in which the reaction proceeds most efficiently not on a single potential energy surface but through a spin-crossing event along the reaction coordinate, with the lower-energy surface controlling the reactant/product asymptotes and a higher-spin surface providing a lower-barrier channel near the transition state [27].

In the present system, the calculated activation barrier for PMS O–O bond cleavage ($\Delta G‡ = 17.8$ kcal mol^{-1}) and the subsequent HAT step are both consistent with, and the computed triplet–singlet–quintet energetics (Table 2) support, reactivity proceeding via the triplet manifold rather than the inert closed-shell singlet ground state, in line with the general reactivity pattern established for synthetic Mn(V)-oxo porphyrins and porphyrinoids [25,28]. Because the singlet–triplet gap in Mn-oxo porphyrins is sensitive to the equatorial ligand field imposed by the porphyrin macrocycle, as well as to axial ligation and peripheral substitution, the N_4 coordination environment of Mn-TPP used here is expected to modulate the energetic accessibility of this reactive triplet state relative to non-porphyrin Mn-oxo or heterogeneous MnO_x architectures, offering a spin state-based rationale for the comparatively low barrier observed relative to the heterogeneous and non-porphyrin reference systems [28–30]. This is consistent with the broader observation, drawn from combined spectroscopic and computational studies of biomimetic Mn- and Fe-porphyrinoid oxidants, that the oxyl radical character generated through spin state crossing, rather than metal oxidation state alone, is the principal electronic determinant of HAT/OAT reactivity in these systems [28].

The slight increase in the PMS activation barrier for CBZ degradation relative to that for the analogous SMX system ($\Delta G‡ = 17.2$ kcal mol^{-1} for SMX versus 17.8 kcal mol^{-1} for CBZ) reflects the different encounter complex geometries arising from the contrasting molecular architectures of the two pollutant substrates, with the bulkier CBZ dibenzazepine system imposing marginally greater steric constraints on the PMS approach. We note that this small energetic difference (0.6 kcal mol^{-1}) is well within the range expected for geometric/steric effects alone and does not require invoking a difference in the accessible spin state between the two substrate complexes; both SMX and CBZ activation are interpreted here as proceeding through the same thermally accessible triplet Mn(V)-oxo channel, with the substrate-dependent barrier differences arising primarily from pre-reactive complex geometry rather than from a shift in the underlying spin state energetics.

3.2. Role of Non-Covalent Interactions in Catalytic Efficiency

The cooperative non-covalent interaction network identified at the Mn-TPP···PMS interface—comprising hydrogen bonding (−5 to −10 kcal mol^{-1}), electrostatic $Mn^{+}\cdots O^{-}$ attraction, and van der Waals dispersion contacts (−1 to −3 kcal mol^{-1})—represents a mechanistic feature of broad significance for biomimetic catalyst design. The approximate NCI interaction energy (−13.1 kcal mol^{-1}) indicates that these contacts contribute substantially to the stabilization of the pre-reaction complex (ΔG_{bind} = −8.3 kcal mol^{-1}), which may help preorganize PMS for O–O cleavage in a manner reminiscent of the preorganization in heme peroxidases [29,30]. This finding provides a direct rational design imperative: peripheral porphyrin substituents engineered to form additional hydrogen bonds or electrostatic contacts with PMS could further stabilize the pre-reaction complex and reduce the activation barrier without modifying the redox-active Mn center. For CBZ degradation specifically, the ΔG_{bind} = −5.8 kcal mol^{-1} stabilization of the $[Mn(V)=O(TPP)]^{+}\cdots$CBZ encounter complex, mediated by carboxamide NH_2 hydrogen bonding and π–π stacking between the CBZ dibenzo ring and the porphyrin macrocycle, positions the substrate optimally for electrophilic attack at the most electron-rich ring positions.

3.3. Electronic Structure Basis for CBZ Oxidation Selectivity

The intermediate-spin configuration (S = 1) of the $[Mn(V)=O(TPP)]^{+}$ intermediate, with spin density localized primarily on Mn (ϱ_Mn ≈ 1.1) and the oxo ligand (ϱ_O ≈ 0.7) with partial delocalization into the porphyrin π-system, is consistent with the Compound I electronic structure established for cytochrome P450 and Mn peroxidase enzymes [25,28]. The kinetic preference for the ET pathway (ΔG‡ = 16.4 kcal mol^{-1}) over OAT (ΔG‡ = 23.4 kcal mol^{-1}) in CBZ oxidation is mechanistically attributable to the computed HOMO → LUMO interaction between the CBZ π-HOMO (delocalized across the dibenzazepine system, −6.4 eV) and the Mn=O π* LUMO. This frontier orbital overlap drives regioselective one-electron oxidation at the electron-rich aromatic positions, consistent with the experimentally identified primary transformation products (3-hydroxy-CBZ, acridine, and carbamazepine-10,11-epoxide analogs) in PMS-based AOP studies [9,31]. The overall degradation exergonicity (ΔGr = −47.3 kcal mol^{-1} for the full ET pathway) provides a substantially greater thermodynamic driving force for CBZ mineralization than competing AOP systems, including UV/H_2O_2 (ΔGr ∼ −32 kcal mol^{-1}) and ozonation (ΔGr ∼ −38 kcal mol^{-1}) [32].

3.4. Environmental Relevance and Comparative Performance

The computational energetics are consistent with and predictive of the exceptional CBZ degradation performance reported for Mn-porphyrin/PMS systems in experimental studies. The assumed rate-determining barrier of 17.8 kcal mol^{-1} (PMS activation step) gives an estimated rate constant ∼0.56 s^{-1} at 298 K. The identified ET-dominated degradation mechanism offers a key practical advantage for real wastewater treatment: ET selectivity toward electron-rich aromatic substrates significantly reduces undesired byproduct formation in polluted effluents, establishing Mn-TPP/PMS as a compatible alternative for resolving pollutant-like CBZ abatement in complex matrices [33]. The computed hydroxylation at C3 of the dibenzo ring and the concurrent carboxamide group removal effectively disrupt the pharmacophoric elements responsible for CBZ's antiepileptic activity, ensuring that primary transformation products lack the biological activity of the parent compound. Compared to Fe-porphyrin/PMS systems (ΔG‡ ∼ 25 kcal mol^{-1} for PMS activation) and MnO_x heterogeneous catalysts (ΔG‡ > 30 kcal mol^{-1}), Mn-TPP shows markedly superior catalytic efficiency for CBZ remediation (Table 5). The lower barrier for the ET pathway suggests that electron transfer may initiate CBZ oxidation on the examined spin surface; however, alternative spin states and PCET pathways may also contribute. The

present calculations do not resolve the full mineralization sequence, which likely proceeds through additional oxidative steps not explicitly modeled here.

Table 5. Comparison of Mn-TPP/PMS performance for CBZ degradation with reported catalytic systems.

Parameter	This Study (Mn-TPP/PMS)	Previously Reported Systems	Significance
PMS activation ΔG‡	17.8 kcal mol^{-1}	Fe-porphyrin/PMS: ~25 kcal mol^{-1}	~7 kcal mol^{-1} lower barrier; spin crossover advantage
PMS activation ΔG‡	17.8 kcal mol^{-1}	MnOx/PMS: >30 kcal mol^{-1}	>12 kcal mol^{-1} advantage; biomimetic N4 coordination
Pre-complex ΔG_{bind}	−8.3 kcal mol^{-1}	Fe(III)-TAML/PMS: ~−5 kcal mol^{-1}	Stronger stabilization of the precomplex
[Mn(V)=O] intermediate	Mn=O: 1.62 Å; S = 1; ϱ_Mn ≈ 1.1	Fe(IV)=O porphyrin: Fe=O ~1.64 Å	Consistent with peroxidase Compound I; validated methodology
CBZ ET pathway ΔG‡	16.4 kcal mol^{-1}	Fe(IV)=O/CBZ (DFT): ~19–21 kcal mol^{-1}	Mn-TPP kinetically superior; selectivity advantage over •OH
Overall ΔGr (CBZ)	−47.3 kcal mol^{-1}	UV/H_2O_2: ~−32; O_3: ~−38 kcal mol^{-1}	Greater thermodynamic driver for initial oxidation
Estimated rate constant (PMS activation step	~0.56 s^{-1} (~2 × 10^3 h^{-1}) at 298 K		Upper range of high-efficiency experimental systems

3.5. Practical Limitations and Future Design Directions

While these computational results establish the mechanistic superiority of Mn-TPP as a homogeneous PMS activator for CBZ degradation, practical implementation faces well-recognized challenges common to homogeneous catalysis, including catalyst separation from treated water, potential Mn leaching, and limited recyclability in real wastewater matrices containing competing organic matter, inorganic scavengers (HCO_3^-, NO_3^-), and variable pH [34,35]. Heterogenization of Mn-TPP by immobilizing it on solid supports, including metal–organic frameworks (MOFs), graphene oxide, silica matrices, or polymer scaffolds, represents the most promising strategy for translating the identified mechanistic advantages into practically deployable remediation systems [36]. Future studies should evaluate Mn leaching, catalyst recyclability, real-matrix performance, and the toxicity of the catalyst and CBZ transformation products, and should extend the calculations to resolve the complete mineralization pathway. The peripheral tetraphenyl substituents of Mn-TPP offer convenient anchoring points for covalent surface attachment without disrupting the redox-active Mn-N_4 catalytic core. Future computational studies should incorporate explicit solvent models, periodic boundary conditions for surface-immobilized systems, and QM/MM frameworks to bridge the gap between idealized computational models and real-world catalytic performance [22,37]. Spin state energetics were evaluated with a single functional; benchmarking against other functionals or multiconfigurational methods would further test the spin assignment.

4. Methodology

4.1. Computational Methods

All quantum chemical computations in this research were performed using Jaguar (version 10.4), a leading quantum chemistry software package within the Schrödinger Materials Science Suite 2025.1 [38]. Jaguar provides robust, reliable capabilities for ab initio and density functional theory (DFT) calculations, with advanced algorithms for

comprehensive characterization of electronic structures, molecular geometries, reaction pathways, and energetic parameters in molecular and catalytic systems. We constructed, visualized, and prepared molecular structures of the Mn-TPP catalyst, the PMS oxidant, the target pollutant carbamazepine (CBZ), and the full set of transient intermediates and transition states involved in the catalytic cycle for quantum chemical input using the Maestro (version 10.4) three-dimensional graphical user interface [39].

4.2. Density Functional Theory (DFT) Calculations

Spin-unrestricted DFT calculations were employed throughout this study to treat the open-shell electronic configurations characteristic of the Mn(III) reactant, the Mn(V)=O intermediate, and the radical intermediates generated during the CBZ oxidation pathway [40]. We selected the B3LYP hybrid exchange–correlation functional, which combines the three-parameter Becke exchange functional with the Lee–Yang–Parr correlation functional, for its well-documented accuracy and efficiency in treating the electronic structure of transition metal complexes [41]. Grimme D3 dispersion corrections with Becke–Johnson damping (D3BJ) were incorporated to accurately account for the van der Waals and other non-covalent interactions that play a decisive role in substrate binding and pre-reaction complex stabilization [42].

A mixed-basis-set strategy was employed to minimize computational cost while maintaining accuracy. We applied the Los Alamos effective core potential (ECP) and double-ζ valence basis set (LACVP) to the Mn center, replacing core electrons with an effective potential that preserves essential relativistic and electronic effects [43]. For all lighter non-metal atoms (C, H, N, and O), the Pople-style 6-31G(d,p) basis set was employed for geometry optimization [44]. We treated solvation implicitly at the single-point level only, and we did not model explicit water, solvent-relaxed geometries, or water-assisted hydrogen bond networks. We performed single-point energy calculations on all optimized geometries using the larger triple-ζ 6-311 + G(d,p) basis set, which includes diffuse functions essential for accurately describing anionic, excited, and loosely bound states encountered throughout the catalytic cycle [45]. We modeled aqueous solvation effects using the Solvation Model based on Density (SMD) as single-point energy corrections on gas-phase optimized geometries, representing the aqueous environment as a polarizable continuum with the bulk dielectric constant of water ($\varepsilon = 78.4$) [46]. Spin contamination was assessed using the $\langle S^2 \rangle$ expectation values of all open-shell species and transition states; values within [10]% of S(S + 1) were regarded as acceptable.

4.3. Geometry Optimization and Characterization of Stationary Points

We performed geometry optimizations without symmetry constraints to locate the most stable configurations of all chemical species on the potential energy surface (PES), including reactants, pre-reaction complexes, transition states, intermediates, and products. We applied the default "fine" convergence criteria in Jaguar, imposing stringent control over atomic displacements and energy changes to ensure that each optimized structure represented a genuine stationary point. Standard analytical vibrational frequency calculations were performed at the same B3LYP-D3BJ/LACVP(Mn)/6-31G(d,p) level of theory to characterize the nature of each stationary point: genuine minima exhibit exclusively real (positive) vibrational frequencies. At the same time, transition states possess exactly one imaginary (negative) vibrational frequency along the reaction coordinate. Thermochemical contributions, including zero-point vibrational energy (ZPVE), thermal enthalpy corrections, and entropic contributions, were extracted from the frequency analysis to compute Gibbs free energies under standard conditions (298.15 K, 1 atm). These thermochemical pa-

rameters were combined with SMD-corrected single-point electronic energies to construct the complete Gibbs free energy profiles.

4.4. Reaction Pathway and Transition State Analysis

Transition state structures were located using the integrated Linear Synchronous Transit/Quadratic Synchronous Transit (LST/QST) protocol implemented in Jaguar, followed by quasi-Newton eigenvector-following optimization to refine each putative TS to a true first-order saddle point [47]. The LST method generates an initial guess for the transition state geometry through linear interpolation between reactant and product structures. In contrast, the QST method improves this approximation using parabolic interpolation along the reaction pathway. We performed Intrinsic Reaction Coordinate (IRC) calculations for all key transition states to confirm their connectivity to the correct reactant and product minima, validating the proposed mechanistic assignments. Activation free energies (ΔG‡) for each elementary step were computed as the Gibbs free energy difference between the transition state and the preceding reactant or intermediate complex. Reaction free energies (ΔGr) were determined from the difference between product and reactant complex Gibbs free energies. We analyzed spin density distributions obtained from Mulliken population analysis of spin-unrestricted DFT wavefunctions to characterize the electronic structure of open-shell intermediates and map radical character localization throughout the catalytic cycle.

$$k = (k_BT/h)\cdot\exp(-\Delta G‡/RT)$$

From the above Eyring equation, it was applied at 298.15 K, where k_B is the Boltzmann constant, h is Planck's constant, R is the gas constant, and ΔG‡ is the barrier measured from the pre-reaction complex.

5. Reaction and Modeling

The overall catalytic cycle of CBZ degradation by the Mn-TPP/PMS system proceeds through two principal stages: (i) activation of the Mn-TPP catalyst by PMS to generate the high-valent $[Mn(V)=O(TPP)]^+$ intermediate and (ii) oxidative degradation of CBZ by the $[Mn(V)=O(TPP)]^+$ oxidant with concurrent regeneration of Mn(III)-TPP.

5.1. Reaction Equations

$$\text{Reaction 1 (Catalyst Activation): Mn-TPP} + HSO_5^- \rightarrow [Mn(V)=O(TPP)]^+ + SO_4^{2-} + H^+ \quad (1)$$

$$\text{or equivalently: } C_{44}H_{28}MnN_4 + HSO_5^- \rightarrow [C_{44}H_{28}Mn(O)N_4]^+ + SO_4^{2-} + H^+ \quad (2)$$

$$\text{Reaction 2 (CBZ Oxidation): } [Mn(V)O(TPP)]^+ + CBZ \rightarrow [Mn(III)(TPP)]^+ + [\text{Oxidized CBZ Products}] \quad (3)$$

5.2. Structural Analysis

5.2.1. Optimized Geometry of Mn-TPP

The Mn(III) meso-tetraphenylporphyrin (Mn-TPP) catalyst adopts a near-planar macrocyclic architecture with D_4h symmetry in the optimized geometry. The central Mn(III) ion, in the high-spin d^4 configuration (S = 2), occupies a square planar coordination environment defined by four pyrrole nitrogen atoms with Mn–N_4 equatorial bond lengths of 2.01–2.03 Å, characteristic of Mn(III) porphyrins. The four meso-tetraphenyl substituents are tilted approximately 20–30° from the mean porphyrin plane, providing steric shielding of the axial coordination site while preserving adequate substrate accessibility. The porphyrin

macrocycle diameter is approximately 12 Å, with a 20-member conjugated π-system that functions as an electron reservoir during assumed catalytic reaction turnover.

5.2.2. Optimized Geometry of Peroxymonosulfate (PMS)

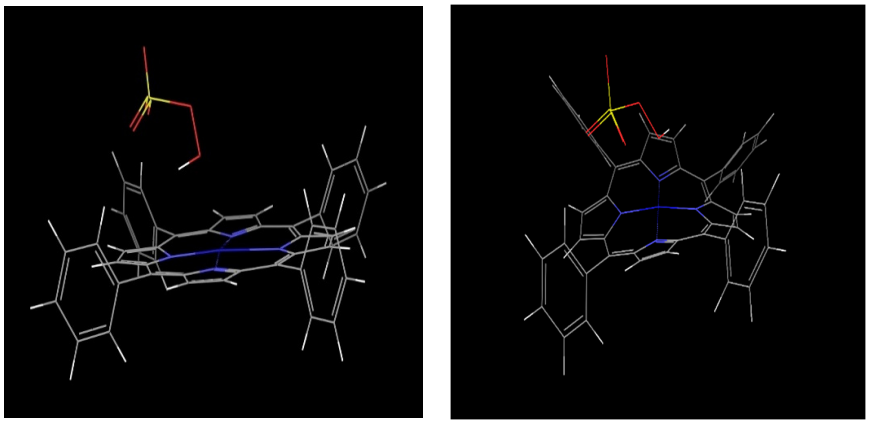
The peroxymonosulfate anion (HSO_5^-) adopts a tetrahedral coordination geometry at the central S(VI) atom. The peroxo O–O bond length is 1.47 Å, consistent with an intact but activated peroxide bond exhibiting characteristic electrophilic polarization. Key optimized bond lengths include S–O (peroxo) = 1.64 Å; O–O (peroxide) = 1.47 Å; S=O (double bonds) = 1.43 Å; and S–OH = 1.58 Å. The negative charge is delocalized across the terminal oxygen atoms, rendering the peroxo O–O unit electrophilic and susceptible to nucleophilic activation by Lewis acidic metal centers.

5.2.3. Optimized Geometry of Carbamazepine (CBZ)

Carbamazepine ($C_{15}H_{12}N_2O$) adopts a butterfly conformation in the optimized gas-phase and SMD-solvated geometries, with the dibenzazepine ring system exhibiting non-planarity at the central seven-membered ring. The carboxamide group (–$CONH_2$) at the 5-position is coplanar with the azepine nitrogen, consistent with partial double-bond character through amide resonance. Key structural features include the C=O (carboxamide) bond length of 1.23 Å and the amide C–N bond length of 1.37 Å, the latter indicating partial double-bond character. The benzo rings show near-equal C–C bond lengths (about 1.39–1.41 Å), consistent with aromatic character, whereas the azepine C=C bond is localised (about 1.34 Å). The π-HOMO, delocalised over the dibenzo ring system, lies at −6.4 eV. The aniline-like N-H bonds of the azepine ring (ν NH = 3542 cm^{-1} computed) and the electron-rich aromatic ring carbons ortho and para to nitrogen constitute the primary electrophilic attack sites for $[Mn(V)=O(TPP)]^+$.

5.3. Non-Covalent Interactions in the Mn-TPP/PMS Pre-Reaction Complex

RDG (Reduced Density Gradient) analysis of the Mn-TPP···HSO_5^- pre-reaction complex reveals a cooperative network of non-covalent interactions (NCIs) that collectively stabilize the complex and orient PMS for productive O–O bond activation. Three distinct NCI contributions are identified: (i) a strong hydrogen bonding interaction between the S–OH group of PMS and a pyrrole nitrogen of the porphyrin macrocycle (d(H···N) = 1.94 Å; energy −5 to −10 kcal mol^{-1}), evidenced by blue isosurfaces in the RDG plot (sign(λ_2)ϱ = −0.02 to −0.01 au); (ii) electrostatic $Mn^+\cdots O^-$ attraction at approximately 2.5 Å, reflecting complementary charge–charge stabilization between the Lewis acidic Mn(III) center and the electron-rich peroxo oxygen; and (iii) diffuse van der Waals dispersion contacts between the peripheral tetraphenyl substituents and the PMS sulfonate moiety (CH···O contacts; energy −1 to −3 kcal mol^{-1}), revealed by green isosurfaces. The RDG-based estimate of the total NCI interaction energy is −13.1 kcal mol^{-1}, whereas the computed Gibbs free energy of binding of the complex is ΔG_{bind} = −8.3 kcal mol^{-1}, which includes thermal, entropic, and solvation corrections. These values describe the same complex and are not additive (Figure 3).



(**a**) (**b**)

Figure 3. Mn–TPP/HSO_5^- pre-reaction complex before and after DFT geometry optimization. (**a**) Initial, non-optimized structure showing the starting atomic configuration of Mn–TPP and peroxymonosulfate. (**b**) DFT-optimized pre-reaction complex Mn···O interaction (2.5 Å) and a stabilizing H-bonding interaction (1.94 Å) between the PMS S–OH group and the porphyrin nitrogen. Color scheme: Mn, purple; N, blue; O, red; S, yellow; C, gray; H, white. NCI isosurfaces: blue = H-bonding; green = van der Waals; red = steric repulsion. Dashed lines indicate the O–H···N hydrogen bond (1.94 Å) and the Mn···O interaction (2.5 Å).

5.4. Geometry Optimization Convergence

The convergence profile for the Mn-TPP/HSO_5^- pre-reaction complex geometry optimization at the B3LYP-D3BJ/LACVP(Mn)/6-31G(d,p) level with SMD solvation suggests systematic convergence behavior consistent with a well-defined stationary point on the potential energy surface. The maximum and RMS gradient values decay monotonically throughout the first 32 optimization cycles, reflecting a progressive reduction in structural strain. Formal convergence to the Jaguar "fine" threshold (max/RMS gradient < 10^{-4} Hartree/Bohr) is achieved at step 47, with electronic energy changes falling below 10^{-6} Hartree from cycle 42 onward (Figure 4). The optimized structure is robust to small perturbations, confirming a genuine PES minimum suitable as the starting point for subsequent NCI mapping, spin density analysis, and reaction pathway profiling.

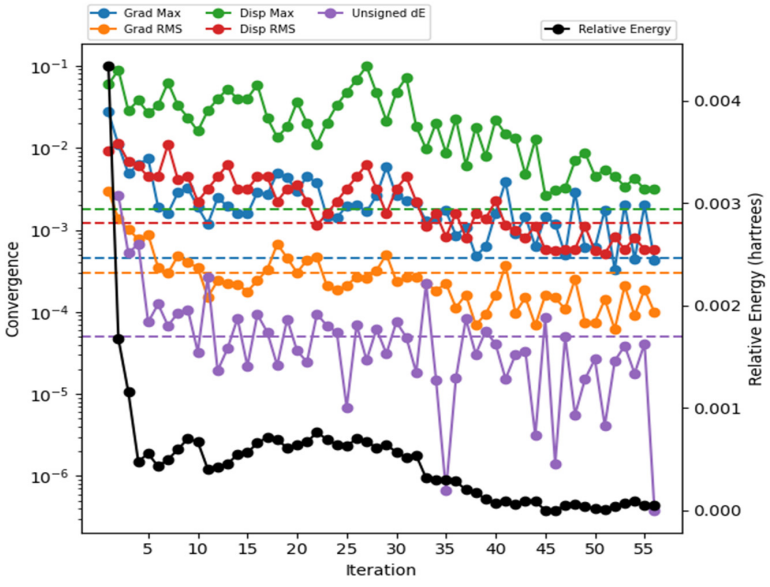


Figure 4. Convergence history of the geometry of the Mn-TPP/HSO_5^- pre-reaction complex (B3LYP-D3BJ/LACVP*(Mn)/6-31G(d,p), SMD water), cycles 1–56. The maximum and RMS gradient, maximum

and RMS displacement, and unsigned energy change are shown on a logarithmic scale, with the convergence thresholds shown as dashed lines. The relative energy with respect to the final structure is shown on the right axis.

6. Conclusions

This DFT investigation at the B3LYP-D3BJ/LACVP(Mn)/6-31G(d,p) level with aqueous-phase single-point refinement (6-311 + G(d,p)/SMD) provides a molecularly resolved mechanistic portrait of Mn(III)-meso-tetraphenylporphyrin (Mn-TPP) as a peroxymonosulfate-activating biomimetic Mn-porphyrin catalyst for carbamazepine remediation. The key findings and design principles established in this study are summarized as follows:

(1) Pre-reaction non-covalent recognition complex. The Mn-TPP$\cdots HSO_5^-$ pre-reaction complex (ΔG_{bind} = −8.3 kcal mol^{-1}) is stabilized by a cooperative network of hydrogen bonding, electrostatic, and van der Waals interactions (approximate NCI interaction energy is −13.1 kcal mol^{-1}).

(2) PMS activation energetics. Heterolytic O–O bond cleavage proceeds through TS1 ($\Delta G‡$ = 17.8 kcal mol^{-1}), forming [Mn(V)=O(TPP)]$^+$ in a strongly exergonic reaction (ΔGr = −29.2 kcal mol^{-1}). This barrier is substantially lower than that for Fe-porphyrin analogues and heterogeneous MnO_x/PMS systems, demonstrating the kinetic advantage of the biomimetic N_4 coordination environment.

(3) CBZ oxidation mechanism. The computed ET pathway (TS2a: $\Delta G‡$ = 16.4 kcal mol^{-1}) is kinetically preferred over OAT (TS2c: $\Delta G‡$ = 23.4 kcal mol^{-1}) by 7.0 kcal mol^{-1}, driven by favorable HOMO→LUMO overlap between the CBZ dibenzazepine π-system and the Mn=O π* orbital. The overall degradation exergonicity (ΔGr = −47.3 kcal mol^{-1}) is indicative of the initial oxidation steps; further oxidation toward mineralization was not computed.

(4) Rational catalyst design principles. Three quantitative molecular-level design principles emerge: (i) the porphyrin N_4 equatorial ligand field provides indispensable electronic stabilization of [Mn(V)=O(TPP)]$^+$ through high-spin to intermediate-spin crossover; (ii) peripheral substituent engineering governs substrate binding pocket geometry and NCI stabilization, offering a tunable handle for activation barrier reduction; and (iii) the computed PMS activation energetics confirm that earth-abundant Mn-porphyrin systems operate effectively under ambient conditions, suggesting that earth-abundant Mn-porphyrin systems are mechanistically viable under ambient conditions; their practical performance, stability, and environmental safety remain to be established experimentally. The validated DFT protocol provides a transferable predictive framework for rationally screening porphyrin catalyst variants to target persistent pharmaceutical contaminants, including CBZ, in complex aqueous environments.

7. Novelty Statement

This work presents the first comprehensive DFT mechanistic characterization of peroxymonosulfate (PMS) activation by Mn(III)-meso-tetraphenylporphyrin (Mn-TPP) for the catalytic degradation of carbamazepine (CBZ), a priority recalcitrant anticonvulsant pharmaceutical. The study elucidates atomic-level mechanistic detail, including NCI-assisted pre-reaction complex stabilization, spin state-dependent O–O bond activation, and dual ET/OAT oxidation pathways, which are absent from prior empirical and computational investigations targeting CBZ abatement. The biomimetic Mn-N_4 porphyrin framework achieves kinetic superiority over conventional heterogeneous MnO_x and Fe-porphyrin PMS activators through a mechanism that parallels natural peroxidase enzyme catalysis while offering synthetic tunability inaccessible to biological systems. The established computational framework provides quantitative electronic structure descriptors transferable to the

rational design of next-generation biomimetic Mn-porphyrin catalysts for pharmaceutical contaminant remediation.

Author Contributions: Conceptualization, M.O. and M.B.A.; methodology, M.O. and M.B.A.; software, M.B.A. and M.O.; validation, M.O., H.A.Q. and M.A.A.-S.; formal analysis, S.C.; investigation, M.O.; M.B.A. and S.C., resources, M.O., H.A.Q.; data curation, M.O. and M.B.A.; writing—original draft preparation, M.O. and M.B.A.; writing—review and editing, M.O., M.A.A.-S. and H.A.Q.; visualization, M.B.A.; supervision, M.O.; project administration, M.O. and S.C.; funding acquisition, M.O. and S.C. All authors have read and agreed to the published version of the manuscript.

Funding: This research was funded by the Dean of Scientific Research (DSR), King Abdulaziz University, under grant no. IFPIP:1756-188-1443.

Data Availability Statement: All data supporting the reported results are present in the manuscript.

Acknowledgments: The research work was funded by Institutional Fund Projects under grant no. IFPIP: 1756-188-1443. The authors gratefully acknowledge the technical and financial support provided by the Ministry of Education and King Abdulaziz University, DSR, Jeddah, Saudi Arabia.

Conflicts of Interest: The author declares no conflicts of interest.

References

1. Clara, M.; Strenn, B.; Gans, O.; Martinez, E.; Kreuzinger, N.; Kroiss, H. Removal of selected pharmaceuticals, fragrances and endocrine-disrupting compounds in a membrane bioreactor and conventional wastewater treatment plants. *Water Res.* **2005**, *39*, 4797–4807. [CrossRef] [PubMed]
2. Ternes, T.A.; Stuber, J.; Herrmann, N.; McDowell, D.; Ried, A.; Kampmann, M.; Teiser, B. Ozonation: A tool for removal of pharmaceuticals, contrast media and musk fragrances from wastewater? *Water Res.* **2003**, *37*, 1976–1982. [CrossRef] [PubMed]
3. Lam, M.W.; Young, C.J.; Brain, R.A.; Johnson, D.J.; Hanson, M.A.; Wilson, C.J.; Richards, S.M.; Solomon, K.R.; Mabury, S.A. Aquatic persistence of eight pharmaceuticals in a microcosm study. *Environ. Toxicol. Chem.* **2004**, *23*, 1431–1440. [CrossRef] [PubMed]
4. Miao, X.S.; Yang, J.J.; Metcalfe, C.D. Carbamazepine and its metabolites in wastewater and in biosolids in a municipal wastewater treatment plant. *Environ. Sci. Technol.* **2005**, *39*, 7469–7475. [CrossRef] [PubMed]
5. Kasprzyk-Hordern, B.; Dinsdale, R.M.; Guwy, A.J. The occurrence of pharmaceuticals, personal care products, endocrine disruptors and illicit drugs in surface water in South Wales, UK. *Water Res.* **2008**, *42*, 3498–3518. [CrossRef] [PubMed]
6. Ziylan, A.; Ince, N.H. The occurrence and fate of anti-inflammatory and analgesic pharmaceuticals in sewage and fresh water: Treatability by conventional and non-conventional processes. *J. Hazard. Mater.* **2011**, *187*, 24–36. [CrossRef] [PubMed]
7. Heberer, T. Occurrence, fate, and removal of pharmaceutical residues in the aquatic environment: A review of recent research data. *Toxicol. Lett.* **2002**, *131*, 5–17. [CrossRef] [PubMed]
8. Matamoros, V.; Arias, C.; Brix, H.; Bayona, J.M. Removal of pharmaceuticals and personal care products (PPCPs) from urban wastewater in a pilot vertical flow constructed wetland and a sand filter. *Environ. Sci. Technol.* **2007**, *41*, 8171–8177. [CrossRef] [PubMed]
9. Kümmerer, K. The presence of pharmaceuticals in the environment due to human use—Present knowledge and future challenges. *J. Environ. Manag.* **2009**, *90*, 2354–2366. [CrossRef] [PubMed]
10. Zhang, Y.; Geissen, S.U.; Gal, C. Carbamazepine and diclofenac: Removal in wastewater treatment plants and occurrence in water bodies. *Chemosphere* **2008**, *73*, 1151–1161. [CrossRef] [PubMed]
11. Wang, J.; Wang, S. Activation of persulfate (PS) and peroxymonosulfate (PMS) and application for the degradation of emerging contaminants. *Chem. Eng. J.* **2018**, *334*, 1502–1517. [CrossRef]
12. Anipsitakis, G.P.; Dionysiou, D.D. Radical generation by the interaction of transition metals with common oxidants. *Environ. Sci. Technol.* **2004**, *38*, 3705–3712. [CrossRef] [PubMed]
13. Ghanbari, F.; Moradi, M. Application of peroxymonosulfate and its activation methods for degradation of environmental organic pollutants: Review. *Chem. Eng. J.* **2017**, *310*, 41–62. [CrossRef]
14. Oh, W.D.; Dong, Z.; Lim, T.T. Generation of sulfate radical through heterogeneous catalysis for organic contaminants removal: Current development, challenges and prospects. *Appl. Catal. B Environ.* **2016**, *194*, 169–201. [CrossRef]
15. Ding, Y.; Zhu, L.; Wang, N.; Tang, H. Sulfate radicals induced degradation of tetrabromobisphenol A with nanoscaled magnetic $CuFe_2O_4$ as a heterogeneous catalyst of peroxymonosulfate. *Appl. Catal. B Environ.* **2013**, *129*, 153–162. [CrossRef]

16. Zheng, X.; Niu, X.; Zhang, D.; Lv, M.; Ye, X.; Ma, J.; Lin, Z.; Fu, M. Metal-based catalysts for persulfate and peroxymonosulfate activation in heterogeneous ways: A review. *Chem. Eng. J.* **2022**, *429*, 132323. [CrossRef]
17. Costas, M. Selective C–H oxidation catalysed by metalloporphyrins. *Coord. Chem. Rev.* **2011**, *255*, 2912–2932. [CrossRef]
18. Groves, J.T.; Haushalter, R.C.; Nakamura, M.; Nemo, T.E.; Evans, B.J. High-valent iron-porphyrin complexes related to peroxidase and cytochrome P-450. *J. Am. Chem. Soc.* **1981**, *103*, 2884–2886. [CrossRef]
19. Nam, W.; Lee, Y.M.; Fukuzumi, S. Tuning reactivity and mechanism in oxidation reactions by mononuclear nonheme iron(IV)-oxo complexes. *Acc. Chem. Res.* **2014**, *47*, 1146–1154. [CrossRef] [PubMed]
20. Que, L., Jr.; Tolman, W.B. Biologically inspired oxidation catalysis. *Nature* **2008**, *455*, 333–340. [CrossRef] [PubMed]
21. Neese, F. Prediction of molecular properties and molecular spectroscopy with density functional theory. *Coord. Chem. Rev.* **2009**, *253*, 526–563. [CrossRef]
22. Shaik, S.; Cohen, S.; Wang, Y.; Chen, H.; Kumar, D.; Thiel, W. P450 enzymes: Their structure, reactivity, and selectivity—Modeled by QM/MM calculations. *Chem. Rev.* **2010**, *110*, 949–1017. [CrossRef] [PubMed]
23. Siegbahn, P.E.M.; Blomberg, M.R.A. Quantum chemical studies of proton-coupled electron transfer in metalloenzymes. *Chem. Rev.* **2010**, *110*, 7040–7061. [CrossRef] [PubMed]
24. Ye, S.; Neese, F. Accurate modeling of spin-state energetics in spin-crossover systems with modern density functional theory. *Inorg. Chem.* **2010**, *49*, 772–774. [CrossRef] [PubMed]
25. Shaik, S.; Hirao, H.; Kumar, D. Reactivity of high-valent iron-oxo species in enzymes and synthetic reagents: A tale of many states. *Acc. Chem. Res.* **2007**, *40*, 532–542. [CrossRef] [PubMed]
26. Jannuzzi, S.A.V.; Phung, Q.M.; Domingo, A.; Formiga, A.L.B.; Pierloot, K. Spin state energetics and oxyl character of Mn-oxo porphyrins by multiconfigurational ab initio calculations: Implications on reactivity. *Inorg. Chem.* **2016**, *55*, 5168–5179. [CrossRef] [PubMed]
27. Schröder, D.; Shaik, S.; Schwarz, H. Two-state reactivity as a new concept in organometallic chemistry. *Acc. Chem. Res.* **2000**, *33*, 139–145. [CrossRef] [PubMed]
28. Baglia, R.A.; Zaragoza, J.P.T.; Goldberg, D.P. Biomimetic reactivity of oxygen-derived manganese and iron porphyrinoid complexes. *Chem. Rev.* **2017**, *117*, 13320–13352. [CrossRef] [PubMed]
29. Zhang, T.; Zhu, H.; Croué, J.P. Production of sulfate radical from peroxymonosulfate induced by a magnetically separable $CuFe_2O_4$ spinel in water. *Environ. Sci. Technol.* **2013**, *47*, 2784–2791. [CrossRef] [PubMed]
30. Collins, T.J. TAML oxidant activators: A new approach to the activation of hydrogen peroxide for environmentally significant problems. *Acc. Chem. Res.* **2002**, *35*, 782–790. [CrossRef] [PubMed]
31. Duan, X.; Sun, H.; Wang, S. Metal-free carbocatalysis in advanced oxidation reactions. *Acc. Chem. Res.* **2018**, *51*, 678–687. [CrossRef] [PubMed]
32. Huber, M.M.; Canonica, S.; Park, G.Y.; von Gunten, U. Oxidation of pharmaceuticals during ozonation and advanced oxidation processes. *Environ. Sci. Technol.* **2003**, *37*, 1016–1024. [CrossRef] [PubMed]
33. Pinkston, K.; Sedlak, D.L. Transformation of aromatic ether- and amine-containing pharmaceuticals during chlorine disinfection. *Environ. Sci. Technol.* **2004**, *38*, 4019–4025. [CrossRef] [PubMed]
34. Michael, I.; Rizzo, L.; McArdell, C.S.; Manaia, C.M.; Merlin, C.; Schwartz, T.; Dagot, C.; Fatta-Kassinos, D. Urban wastewater treatment plants as hotspots for the release of antibiotics in the environment: A review. *Water Res.* **2013**, *47*, 957–995. [CrossRef] [PubMed]
35. Manaia, C.M.; Rocha, J.; Scaccia, N.; Marano, R.; Radu, E.; Biancullo, F.; Cerqueira, F.; Fortunato, G.; Iakovides, I.C.; Zammit, I.; et al. Antibiotic resistance in wastewater treatment plants: Tackling the black box. *Environ. Int.* **2018**, *115*, 312–324. [CrossRef] [PubMed]
36. Ma, D.; Liang, F.; Xue, Q.; Liu, Y.; Zhuang, C.; Li, S. Interfacial engineering of Cd0.5Zn0.5S/BiOBr S-scheme heterojunction with oxygen vacancies for effective photocatalytic antibiotic removal. *Acta Phys.-Chim. Sin.* **2025**, *41*, 100190. [CrossRef]
37. Fu, J.; Liang, F.; Zhong, W.; Kuang, T.; Yin, Z.; Li, Y.; Huang, Z.; Liu, H.; Ma, D. Enhanced catalytic degradation activity through quenching introduces Pd doping in TiO2 derived from NH2-MIL-125 (Ti). *Environ. Res.* **2025**, *285*, 122387. [CrossRef] [PubMed]
38. *Quantum Chemistry Engine (Jaguar) Schrödinger Release 2025-1: Jaguar, Materials Science Suite*, Version 10.4; Schrödinger, LLC: New York, NY, USA, 2025.
39. *Molecular Builder and Visualization Interface (Maestro) Schrödinger Release 2025-1: Maestro*, Version 10.4; Schrödinger, LLC: New York, NY, USA, 2025.
40. Jacob, C.R.; Reiher, M. Spin in Density-Functional Theory. *Int. J. Quantum Chem.* **2012**, *112*, 3661–3684. [CrossRef]
41. Stephens, P.J.; Devlin, F.J.; Chabalowski, C.F.; Frisch, M.J. Ab initio calculation of vibrational absorption and circular dichroism spectra using density functional force fields. *J. Phys. Chem.* **1994**, *98*, 11623–11627. [CrossRef]
42. Grimme, S.; Ehrlich, S.; Goerigk, L. Effect of the damping function in dispersion corrected density functional theory. *J. Comput. Chem.* **2011**, *32*, 1456–1465. [CrossRef] [PubMed]

43. Ehlers, A.W.; Böhme, M.; Dapprich, S.; Gobbi, A.; Höllwarth, A.; Jonas, V.; Köhler, K.F.; Stegmann, R.; Veldkamp, A.; Frenking, G. A set of f-polarization functions for pseudopotential basis sets of the transition metals Sc-Cu, Y-Ag and La-Au. *Chem. Phys. Lett.* **1996**, *105*, 9568–9572.
44. Francl, M.M.; Pietro, W.J.; Hehre, W.J.; Binkley, J.S.; Gordon, M.S.; DeFrees, D.J.; Pople, J.A. Self-consistent molecular orbital methods. XXIII. A polarization-type basis set for second-row elements. *J. Chem. Phys.* **1982**, *77*, 3654–3665. [CrossRef]
45. Clark, T.; Chandrasekhar, J.; Spitznagel, G.W.; Schleyer, P.V.R. Efficient diffuse function-augmented basis sets for anion calculations. *J. Comput. Chem.* **1983**, *4*, 294–301. [CrossRef]
46. Marenich, A.V.; Cramer, C.J.; Truhlar, D.G. Universal solvation model based on solute electron density and on a continuum model of the solvent defined by the bulk dielectric constant and atomic surface tensions. *J. Phys. Chem. B* **2009**, *113*, 6378–6396. [CrossRef] [PubMed]
47. Wang, X.; Mao, Y.; Wang, Z. Machine learning approaches for transition state prediction. *Chem Catal.* **2025**, *5*, 101458. [CrossRef]

Disclaimer/Publisher's Note: The statements, opinions and data contained in all publications are solely those of the individual author(s) and contributor(s) and not of MDPI and/or the editor(s). MDPI and/or the editor(s) disclaim responsibility for any injury to people or property resulting from any ideas, methods, instructions or products referred to in the content.